Geophysical Research Letters

Supporting Information for

Anatomy of the tsunami and Lamb waves-induced ionospheric signatures generated by the 2022 Hunga Tonga volcanic eruption

E. Munaibari[1], L. Rolland[1], A. Sladen[1], B. Delouis[1]

1 – Université Côte d'Azur, Observatoire de la Côte d'Azur, CNRS, IRD, Géoazur, 250 rue Albert Einstein, Sophia Antipolis 06560 Valbonne, France, edhah.munaibari@geoazur.unice.fr

Contents of this file

Introduction

The supplementary material consists of Text S1 & S2, Table S3 and Figures S4 – S15.

Figure S4 illustrates the slant total electron content (sTEC) processing steps to highlight possible tsunami-generated signatures. The figure is supporting Text S2.

Figure S5 shows the Tonga tsunami ionospheric imprints identified in the vicinity of Wallis & Futuna Islands as detected by FTNA GNSS receiver (a) and the map of the positions of the GNSS receiver and the satellites' ionospheric tracks (b). The figure is supporting the bottom subfigure of Figure 1 in the main text.

Figure S6 presents the Tonga tsunami ionospheric imprints identified in the vicinity of Tuvalu Island as detected by TUVA GNSS receiver (a) and the map of the positions of the volcano, the

GNSS receiver and the satellites' ionospheric tracks (b). The figure is supporting the bottom subfigure of Figure 1 in the main text.

Figure S7 displays the Tonga tsunami ionospheric imprints identified in the vicinity of Cook Islands as detected by CKIS GNSS receiver (a) and the map of the positions of the volcano, the GNSS receiver and the satellites' ionospheric tracks (b). The figure is supporting the bottom subfigure of Figure 1 in the main text.

Figure S8 depicts the Tonga tsunami ionospheric imprints identified in the vicinity of Vanuatu Islands as detected by PTVL GNSS receiver (a) and the map of the positions of the volcano, the GNSS receiver and the satellites' ionospheric tracks (b). The figure is supporting the bottom subfigure of Figure 1 in the main text.

Figure S9 displays the Tonga tsunami ionospheric imprints identified in the vicinity of Norfolk Island as detected by NORF GNSS receiver (a) and the map of the positions of the volcano, the GNSS receiver and the satellites' ionospheric tracks (b). The figure is supporting the bottom subfigure of Figure 1 in the main text.

Figure S10 portrays the Tonga tsunami ionospheric imprints identified in the vicinity of northwest New Zealand as detected by KTIA GNSS receiver (a) and the map of the positions of the volcano, the GNSS receiver and the satellites' ionospheric tracks (b). The figure is supporting the bottom subfigure of Figure 1 in the main text.

Figure S11 shows the Tonga tsunami ionospheric imprints identified in the vicinity of Tahiti as detected by FAA1 GNSS receiver (a) and the map of the positions of the GNSS receiver and the satellites' ionospheric tracks (b). The figure is supporting the bottom subfigure of Figure 1 in the main text.

Figure S12 portrays the Tonga tsunami ionospheric imprints identified in the vicinity of southern New Zealand as detected by BLUF GNSS receiver (a) and the map of the positions of the GNSS receiver and the satellites' ionospheric tracks (b). The figure is supporting the bottom subfigure of Figure 1 in the main text.

Figure S13 depicts the Tonga tsunami ionospheric imprints identified in the vicinity of Gambier Islands as detected by GAMB GNSS receiver (a) and the map of the positions of the GNSS receiver and the satellites' ionospheric tracks (b). The figure is supporting the bottom subfigure of Figure 1 in the main text.

Figure S14 displays the Tonga tsunami ionospheric imprints identified in the vicinity of Hawaii Islands as seen by KKAI GNSS receiver (a) and the map of the positions of the GNSS receiver and the satellites' ionospheric tracks (b). The figure is supporting the bottom subfigure of Figure 1 in the main text.

Figure S15 shows the Tonga tsunami ionospheric imprints identified in the vicinity of Galapagos Islands as detected by GLPS GNSS receiver (a) and the map of the positions of the GNSS receiver and the satellites' ionospheric tracks (b). The figure is supporting the bottom subfigure of Figure 1 in the main text.

Figure S16 depicts raw ionospheric measurements during the eruption of the HTHH volcano to highlight the accompanied massive sTEC decreases and increases that resemble a large W-shape.

All GNSS data are freely available from the Geoscience Australia data archives (ftp://ftp.data.gnss.ga.gov.au/daily/) and the CDDIS data archives (https://cddis.nasa.gov/Data_and_Derived_Products/GNSS/daily_30second_data.html). The ocean bathymetry data ETOPO1 (1-minute global relief model; Amante and Eakins 2009) and the open-ocean sea-level measurements (DART) are from the NOAA data archives (https://www.ngdc.noaa.gov/mgg/bathymetry/relief.html; https://www.ngdc.noaa.gov/hazard/DARTData.shtml). The coastal sea-level measurements (tide gauge) are publicly available via the Intergovernmental Oceanographic Commission of UNESCO (http://www.ioc-sealevelmonitor- ing.org/). To generate the tsunami travel times, we take advantage of Geoware TTT SDK software (Wessel, 2009).

Text S1

TEC, which stands for ionospheric total electron content, is a parameter commonly used to study and investigate the state of the ionosphere (Ratcliffe, 1951a, 1951b), which is the layer containing the ionized part of Earth's upper atmosphere and stretches from approximately 50 km to more than 1000 km. The established definition of the total electron content is the total number of electrons integrated between two points along a column of a meter-squared cross-section according to the following expression

$$TEC = \int n_e(s)\, ds$$

where ds is the integration path and $n_e(s)$ in the location-dependent electron density (Evans, 1957). Before going into how TEC is computed from observations and how it's related to the detection of Tsunamis, a brief look of the theoretical work describing ionospheric disturbances and their driving mechanism is presented.

In 1960, Hines put forward the initial theory describing the cause of ionospheric disturbances. In his theory, Hines (1960) attributed such disturbances to internal atmospheric gravity waves generated in lower regions of the atmosphere and propagated upward to the ionosphere. The theory was then affirmed by the work of Hooke (1969) and Davis (1973) where they studied and analyzed the behavior of electron and ion densities and the integrated ionospheric response (TEC) to internal atmospheric gravity waves, respectively. Within the same time period, it was suggested that surface disturbances such as earthquakes and tsunamis produce internal atmospheric gravity waves (Donn & Posmentier, 1964; Hines, 1972) that travel upward to ionospheric heights imprinting an identifiable signature in the ionosphere. Such suggestion was then expanded upon by Peltier & Hines (1976) where they assessed the different difficulties in detecting the surface disturbances tsunamis ionospheric signature and confirmed the possibility of observing such signature in the TEC.

There are different methods that are developed to obtain ionospheric TEC measurements from observations such as the Faraday Rotation effect on a linear polarized propagating plane wave (Titheridge, 1972). However, today TEC measurements are made mostly using GNSS (Global Navigation Satellite Systems) data. By utilizing the delay imposed by the ionosphere on the

signal sent by a satellite, TEC values can be computed. For example, in the case of satellites equipped with dual-frequency systems, the ionospheric delay in meters is found according to

$$I = \frac{40.3\ (f_1^2 - f_2^2)}{f_1^2 f_2^2}\ 10^{16}\ TEC$$

where I can be computed by taking the difference of the two measurements of pseudorange or that of carrier phase obtained by a GNSS receiver station and f_1& f_2 are the two frequencies used by the satellites to transmit signals back to the ground stations (Liu et al., 1996).

The first observation using TEC of an ionospheric signature of a surface disturbance was illustrated by Calais & Minster (1995) for the January 17, 1994, Mw=6.7 Northridge earthquake. As for the ionospheric (TEC) signature of a tsunami, Artru et al. (2005) presented the first observations using the dense Japanese GPS Earth Observation Network (GEONET) for the tsunami generated by the 23 June 2001 earthquake in Peru as it approached Japan. After this pioneering observations, several similar observations were made for other events such as the 26 December 2004 Indian Ocean tsunami (Liu et al., 2006), the 15 November 2006 at Kuril Islands, the 29 September 2009 at Samoa Islands, and the 27 February 2010 at Chile (Rolland et al.,2010).

Text S2

To compute the total electron content (TEC), we use a modified version of GNSS-TEC software (Zhivetiev, 2019). In order to highlight possible tsunami-generated signatures, we process the obtained TEC measurements (Fig. S4). The processing involves the removal of longer period variations in TEC time series (such as diurnal variations and multiple hour trends due to changing elevation angle of the receiver-satellite line of sight) as well as constant receivers/satellites instrumental biases. We carry out the removal by detrending the TEC time series with a polynomial of degree 10 after Galvan et al. (2011) (Fig. S4b), followed by performing apodization with a Hann-window taper to minimize edge effects (Fig. S4c). Then to enhance the tsunami-induced imprints, we apply to the time series a Butterworth band-pass filter with order 3 and frequency limits of 0.7 and 3 mHz (the selection of the filter limits is to encapsulate the range where the frequency of the tsunami waves is expected to be, Rolland et al., 2010) (Fig. S4d). The geolocation of the processed TEC measurements in the ionosphere is based on the thin shell assumption (Davies & Hartmann, 1997). The intersection of the line of sight between a GNSS receiver and a satellite with the ionosphere shell at a certain altitude is known as an ionospheric pierce point or IPP. Within this work, we calculate the IPPs at 300 km altitude as the height of the maximum ionospheric electron density set to be between 200 and 400 km (Zhang et al., 1999).

Table S3: Tsunami TEC amplitude of the ten satellite-receiver pairs ionospheric measurements depicted in Figure 1, along with the local tsunami arrival time at both IPPs' and receivers' locations and ionospheric background activity. The tsunami wave height obtained from the closest tide gauge to each receiver is presented in the last column.

TEC series	Receiver location	Tsunami TEC amplitude (TECU)		Ionospheric background✦ (TECU)	Local tsunami arrival time (TAT)		Tsunami wave height*	
		sTEC	vTEC	vTEC	IPP	GNSS receiver	Height† (m)	Tide gauge code
C23-FTNA	Wallis & Futuna Islands (14.308°S 178.121°W)	0.88	0.49	21.35	2022-01-14 18:04:29	2022-01-15 17:38:41	0.02	wall
J03-TUVA	Tuvalu Island (8.525°S 179.197°E)	0.56	0.34	27.76	2022-01-15 18:54:00	2022-01-15 18:45:22	0.12	fong
G12-CKIS	Cook Islands (21.201°S 159.801°W)	0.97	0.39	25.15	2022-01-14 20:58:29	2022-01-14 20:24:48	0.663	raro
G32-PTVL	Vanuatu Islands (17.749°S 168.315°E)	0.79	0.50	23.76	2022-01-15 18:05:00	2022-01-15 18:19:10	1.006	vanu
C01-NORF	Norfolk Island (29.043°S 167.939°E)	0.67	0.40	21.32	2022-01-15 18:30:30	2022-01-15 19:19:55	1.297	kjni
G32-KTIA	New Zealand (35.069°S 173.273°E)	0.73	0.56	17.51	2022-01-15 19:39:30	2022-01-15 20:28:25	0.692	ncpt
C20-LORD	Lord Howe Island (31.520°S 159.061°E)	0.71	0.51	19.29	2022-01-15 20:24:00	2022-01-15 20:08:11	0.668	gcsb
G12-FAA1	Tahiti (17.555°S 149.614°W)	0.72	0.26	25.97	2022-01-14 22:14:29	2022-01-14 21:53:48	0.296	pape
G32-BLUF	New Zealand (46.585°S 168.292°E)	0.33	0.19	15.17	2022-01-15 19:53:00	2022-01-15 21:39:05	0.107	puyt
G29-GAMB	Gambier Islands (23.130°S 134.965°W)	0.47	0.25	21.32	2022-01-15 01:09:59	2022-01-15 00:45:24	0.227	gamb
R21-KKAI	Hawaii Islands (19.066°N 155.799°W)	0.28	0.12	6.96	2022-01-15 00:56:59	2022-01-15 00:31:01	0.392	hilo2
E03-GLPS	Galapagos Islands (0.743°S 90.304°W)	0.98	0.64	42.81	2022-01-15 11:18:29	2022-01-15 11:18:15	0.864	sant

✦ Values extracted from the archives of Project "Ionospheric Weather" of IZMIRAN: Pushkov Institute of Terrestrial Magnetism, Ionosphere and Radio Wave Propagation Russian Academy of Sciences (https://www.izmiran.ru/ionosphere/weather/)

*Tsunami wave height is obtained from the closest tide gauge station to the GNSS receiver.

†The height is calculated within 6-hour observation window starting 1 hour before TAT as $\frac{max_{obs\_w} - min_{obs\_w}}{2}$, after detrending the raw measurements with polynomial of degree 10.

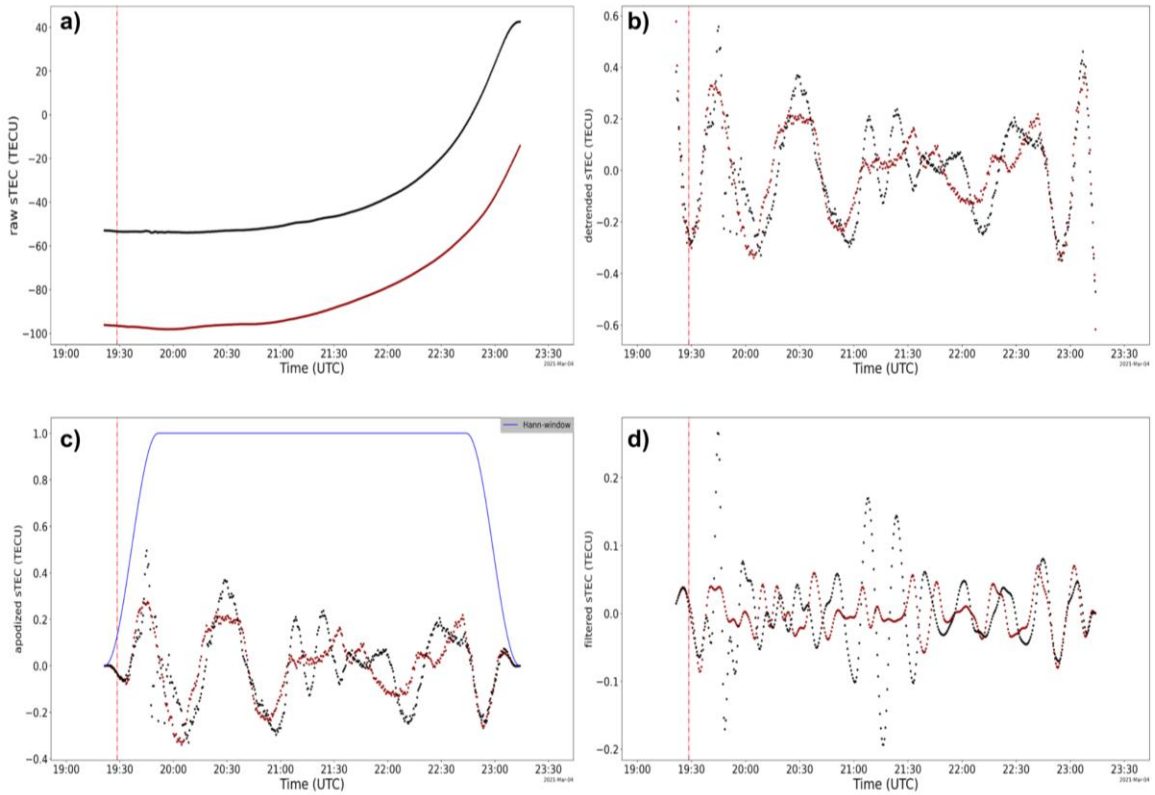

Figure S4. The processing steps of the slant total electron content (sTEC) to highlight possible tsunami-generated signatures: **(a)** raw, **(b)** detrended, **(c)** apodized, and **(d)** band-pass filtered sTEC.

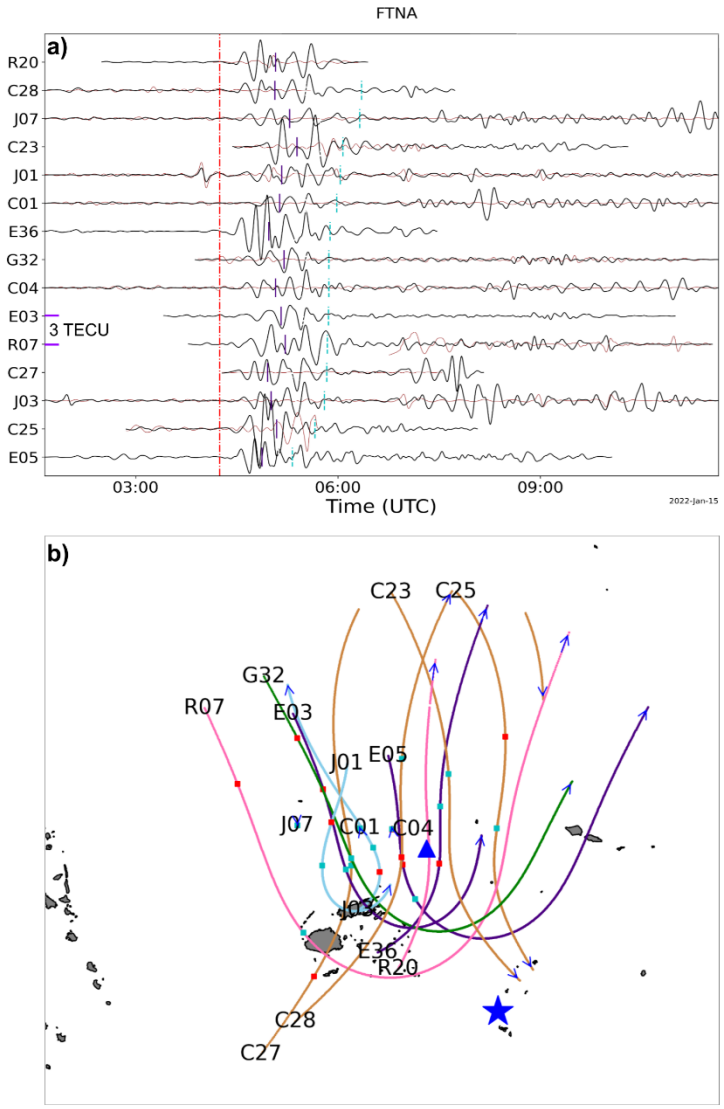

Figure S5. (a) The tsunami-induced ionospheric signatures detected in the vicinity of Wallis & Futuna Islands (FTNA GNSS receiver) following the passage of the tsunami triggered the Jan. 15, 2022 HTHH volcanic eruption. The y axis indicates the satellites ID where the sTEC time series are arranged (bottom to top) according to the tsunami expected arrival time (vertical red dashed lines). The violet vertical solid lines indicate the arrival time of the Lamb (pressure) with traveling speed of 318 m/s, while the vertical green dotted line illustrate the arrival time of a gravity wave (generated by tsunami waves of constant speed as a result of unchanging ocean depth of 5 km) with traveling speed of 221 m/s. **(b)** Geographic view showing the volcano (yellow star), the GNSS receiver (red triangle) and the ionospheric tracks of the satellites (green: GPS, cyan: GLONASS, violet: Galileo, orange: Beidou, skyblue: QZSS) whose sTEC time series are show in (a) with black curves representing the event day data and blue curves denoting that of the day before. Along the satellites' tracks, the pink squares indicate the satellites' locations at the time of the eruption (vertical pink dashdotted line in a), while the red squares point out the satellites' locations at the tsunami expected arrival time (vertical red dashed lines in a). Due to the

close proximity to the volcano, the imprints of the tsunami appears to be mixed with that of the other atmospheric waves (e.g. Lamb wave) triggered by the eruption.

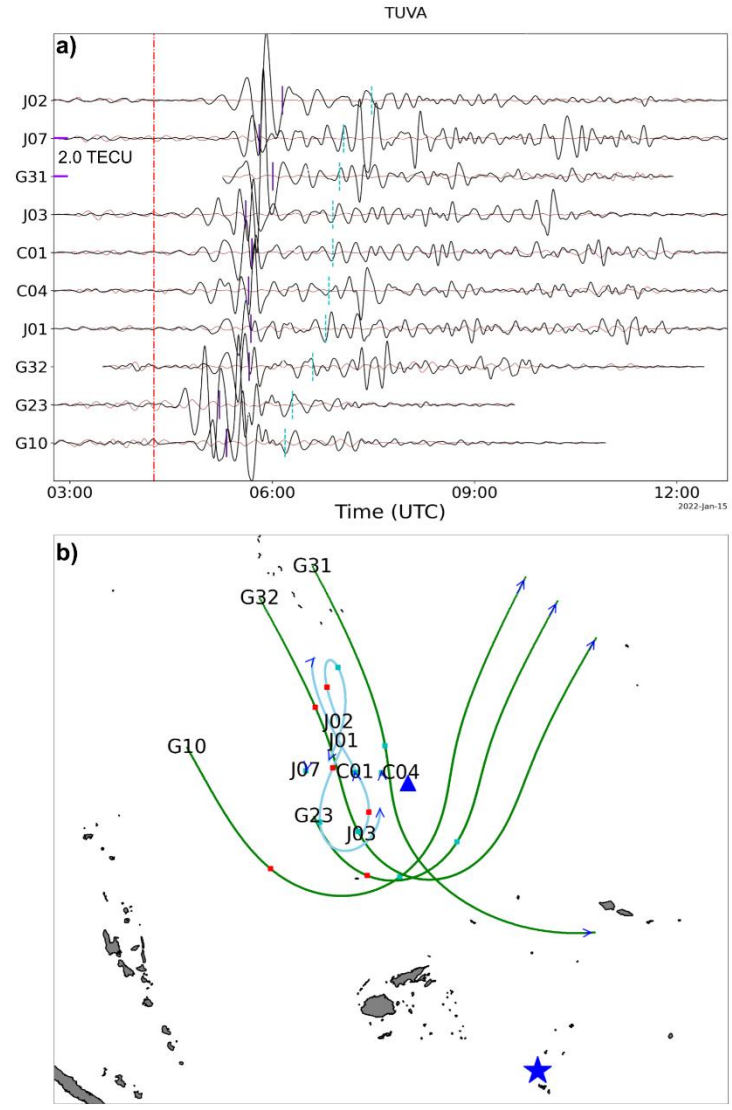

Figure S6. (a) The tsunami-induced ionospheric signatures detected in the vicinity of Tuvalu Island (TUVA GNSS receiver) following the passage of the tsunami triggered the HTHH volcanic eruption. **(b)** Geographic view of the volcano, the GNSS receiver and the ionospheric tracks of the satellites. The ionospheric imprints of the Lamb wave and the tsunami are visible and distinguishable.

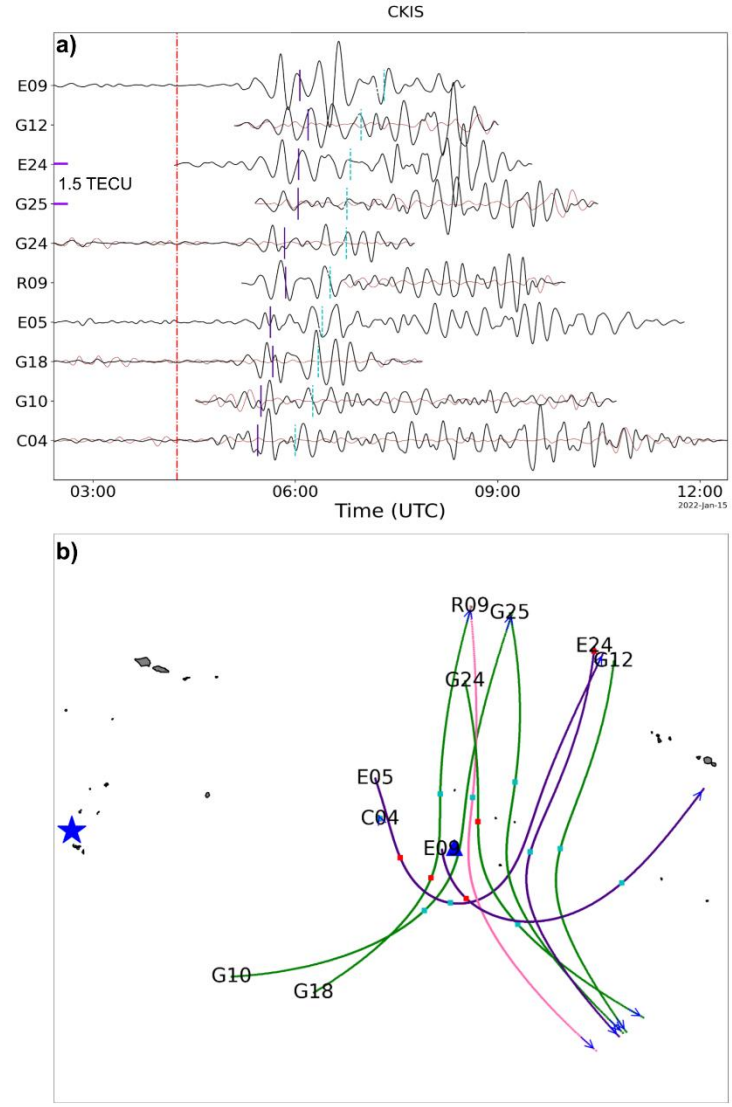

Figure S7. (a) The tsunami-induced ionospheric signatures detected in the vicinity of Cook Islands (CKIS GNSS receiver) following the passage of the tsunami triggered the HTHH volcanic eruption. **(b)** Geographic view of the volcano, the GNSS receiver and the ionospheric tracks of the satellites whose sTEC time series are show in (a). Like the two prior receivers, the ionospheric imprints of the Lamb wave and the tsunami are visible and distinguishable.

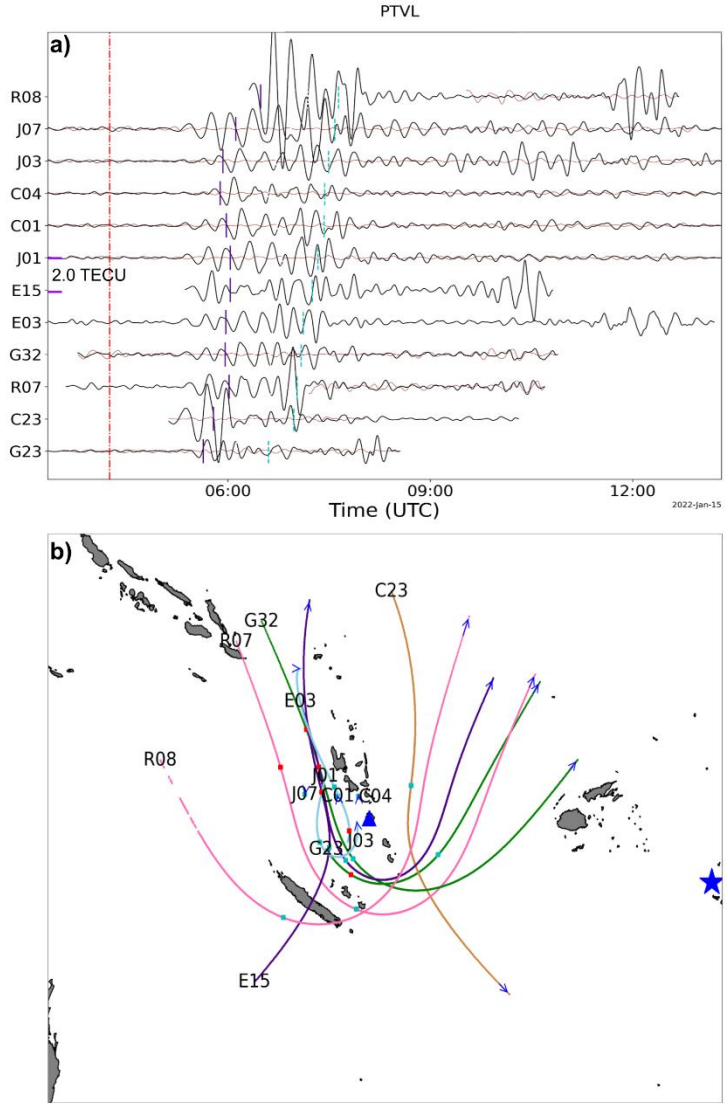

Figure S8. (a) The tsunami-induced ionospheric signatures detected in the vicinity of Vanuatu Islands (PTVL GNSS receiver) following the passage of the tsunami triggered the HTHH volcanic eruption. **(b)** Geographic view of the volcano, the GNSS receiver and the ionospheric tracks of the satellites whose sTEC time series are show in (a). Like the previous cases, we can easily separate the imprints of the Lamb wave from the tsunami's

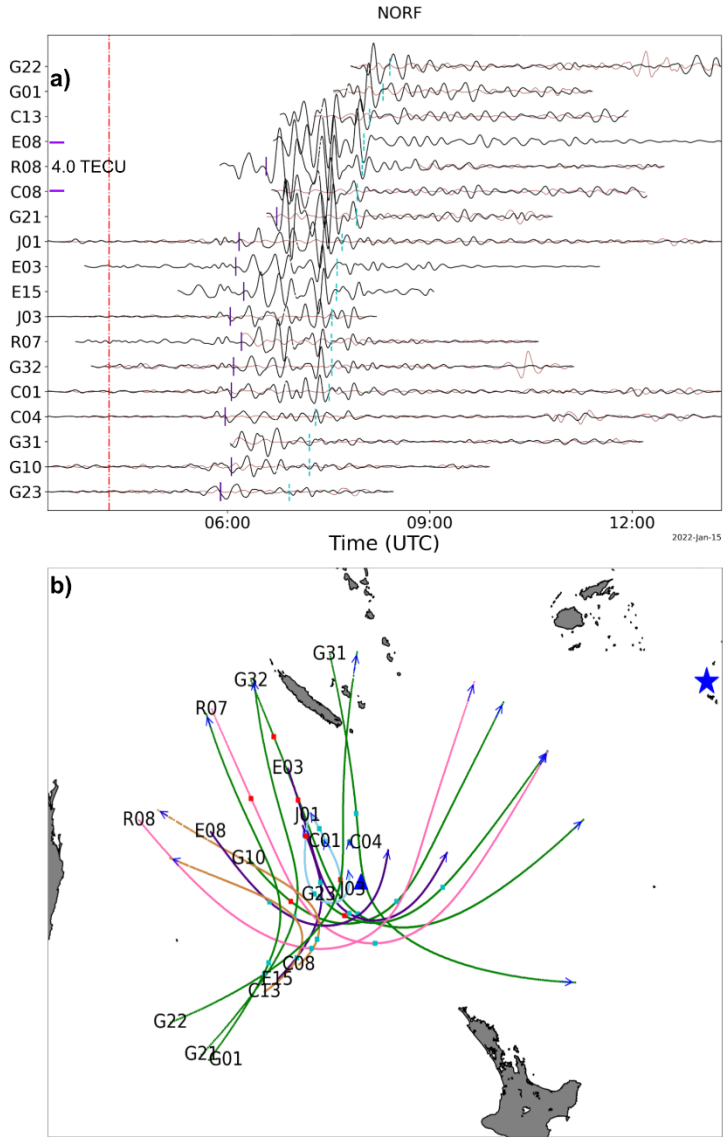

Figure S9. (a) The tsunami-induced ionospheric signatures detected in the vicinity of Norfolk Island (NORF GNSS receiver) following the passage of the tsunami triggered the HTHH volcanic eruption. The eurption time is indicated by the vertical pink dashdotted line. **(b)** Geographic view of the volcano, the GNSS receiver and the ionospheric tracks of the satellites whose sTEC time series are show in (a). One can see clearly the presence of three waves' arrivals; the Lamb wave induced, the constant traveling tsunami induced and the bathymetric tsunami induced.

.

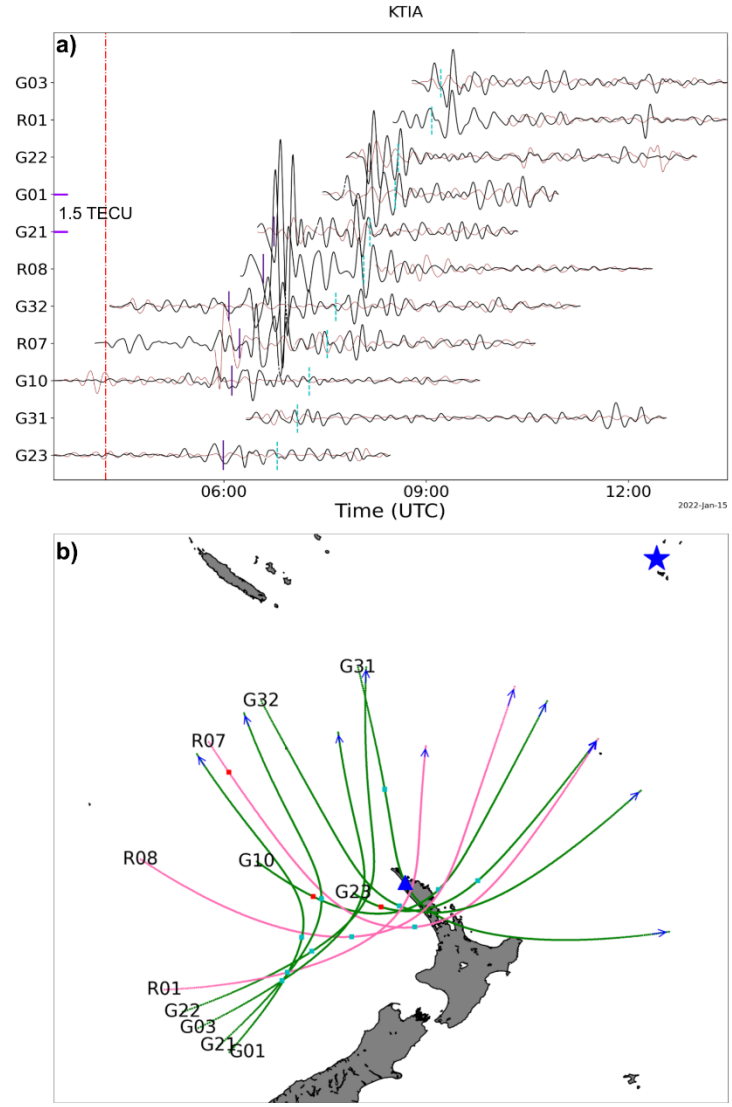

Figure S10. (a) The tsunami-induced ionospheric signatures detected in the vicinity of northwest New Zealand (KTIA GNSS receiver) following the passage of the tsunami triggered the HTHH volcanic eruption. **(b)** Geographic view of the volcano the GNSS receiver and the ionospheric tracks of the satellites whose sTEC time series are show in (a). The results showing here resemble that of PTVL receiver case.

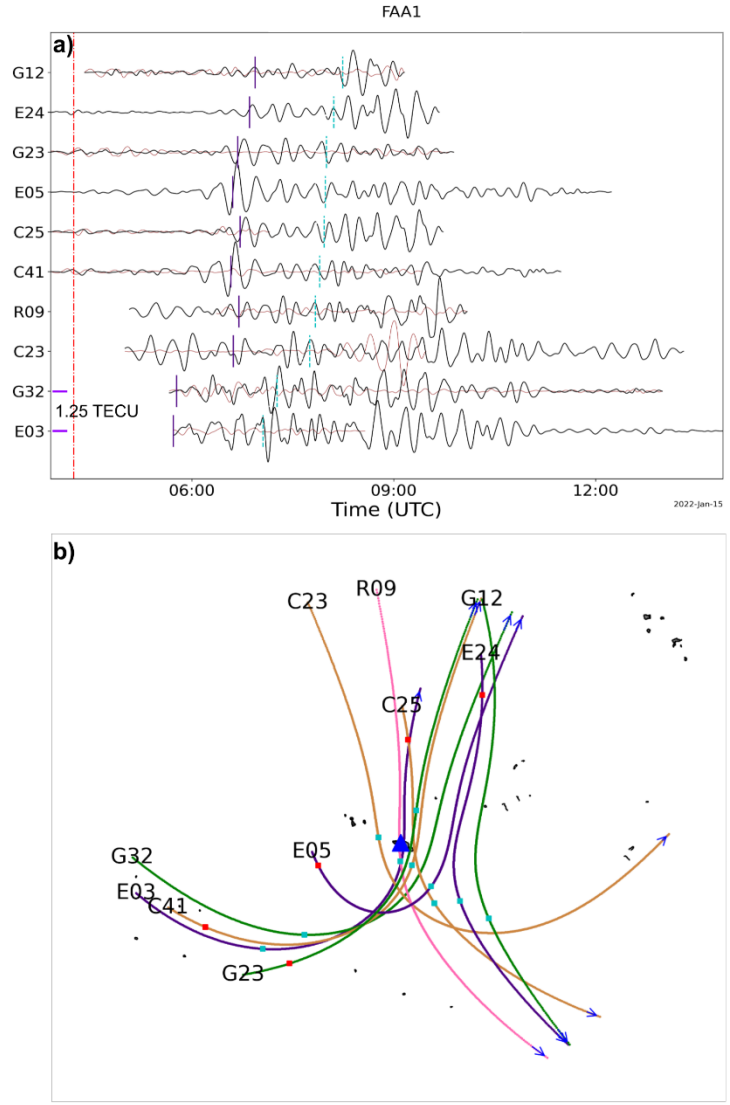

Figure S11. (a) The tsunami-induced ionospheric signatures detected in the vicinity of Tahiti (FAA1 GNSS receiver) following the passage of the tsunami triggered the HTHH volcanic eruption. **(b)** Geographic view of the GNSS receiver and the ionospheric tracks of the satellites whose sTEC time series are show in (a). Due to the distance increase and the different traveling speed of the waves, the tsunami imprints appear to be more visible and less contaminated by the other waves, the eruption injected in the atmosphere.

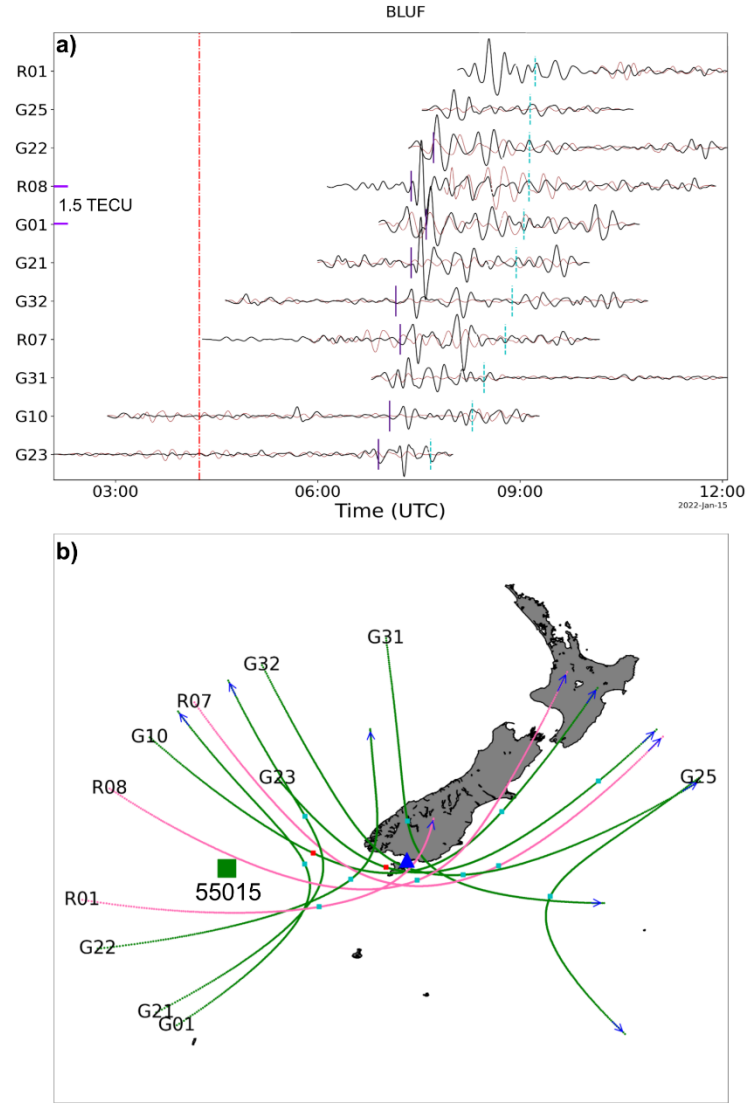

Figure S12. (a) The tsunami-induced ionospheric signatures detected in the vicinity of southern New Zealand (BLUF GNSS receiver) following the passage of the tsunami triggered the HTHH volcanic eruption. **(b)** Geographic view of the GNSS receiver and the ionospheric tracks of the satellites whose sTEC time series are show in (a). Similar to the previous case, the tsunami imprints appear to be more visible and less contaminated by the other waves, the eruption injected in the atmosphere. The black square depicts the position of the tsunami buoy (DART 55015) used in Section 3.4 of the main text.

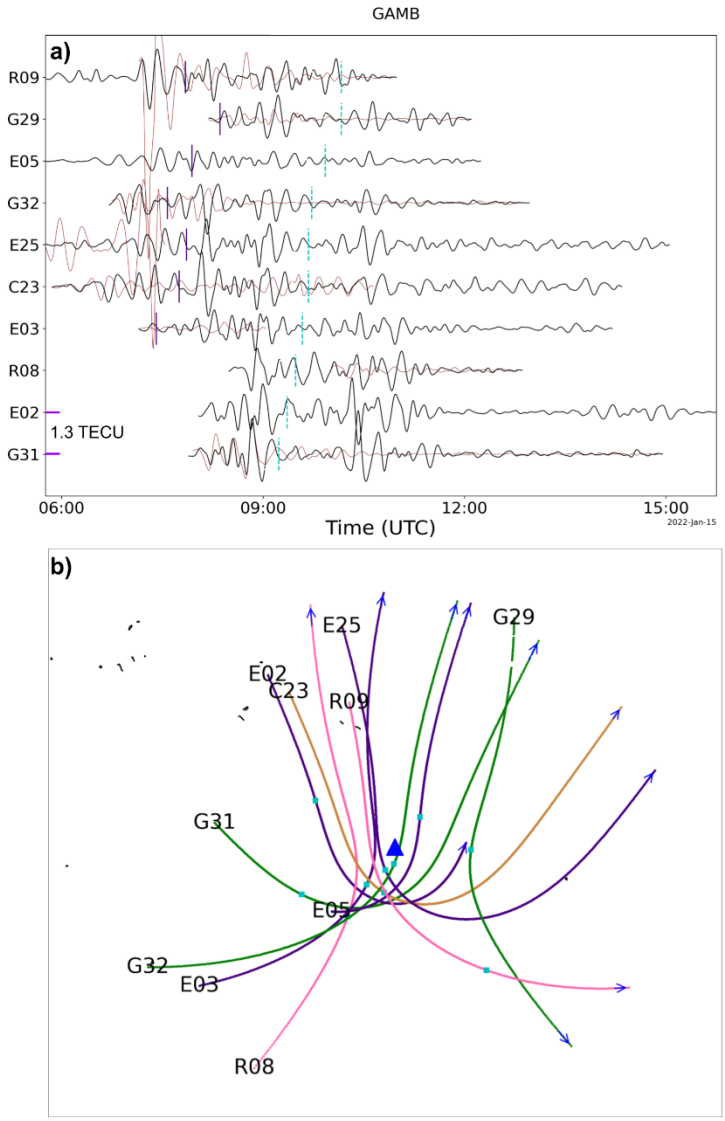

Figure S13. (a) The tsunami-induced ionospheric signatures detected in the vicinity of Gambier Islands (GAMB GNSS receiver) following the passage of the tsunami triggered the HTHH volcanic eruption. **(b)** Map of the GNSS receiver and the ionospheric tracks of the satellites whose sTEC time series are show in (a). With the distance increase, the imprints of the other atmospheric are well separated from that of the tsunami and all appear at their expected times.

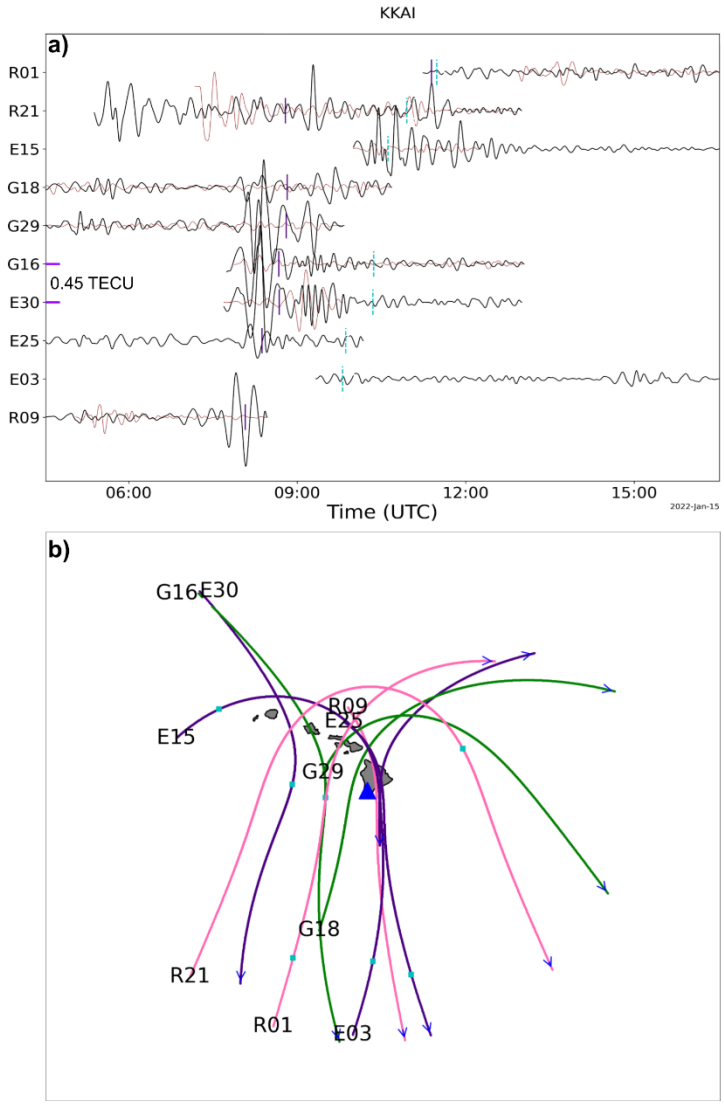

Figure S14. (a) The tsunami-induced ionospheric signatures detected in the vicinity of Hawaii Islands (KKAI GNSS receiver) following the passage of the tsunami triggered the HTHH volcanic eruption. **(b)** Map of the GNSS receiver and the ionospheric tracks of the satellites whose sTEC time series are show in (a). Both the ionospheric signatures of the Lamb wave and the tsunami are visible.

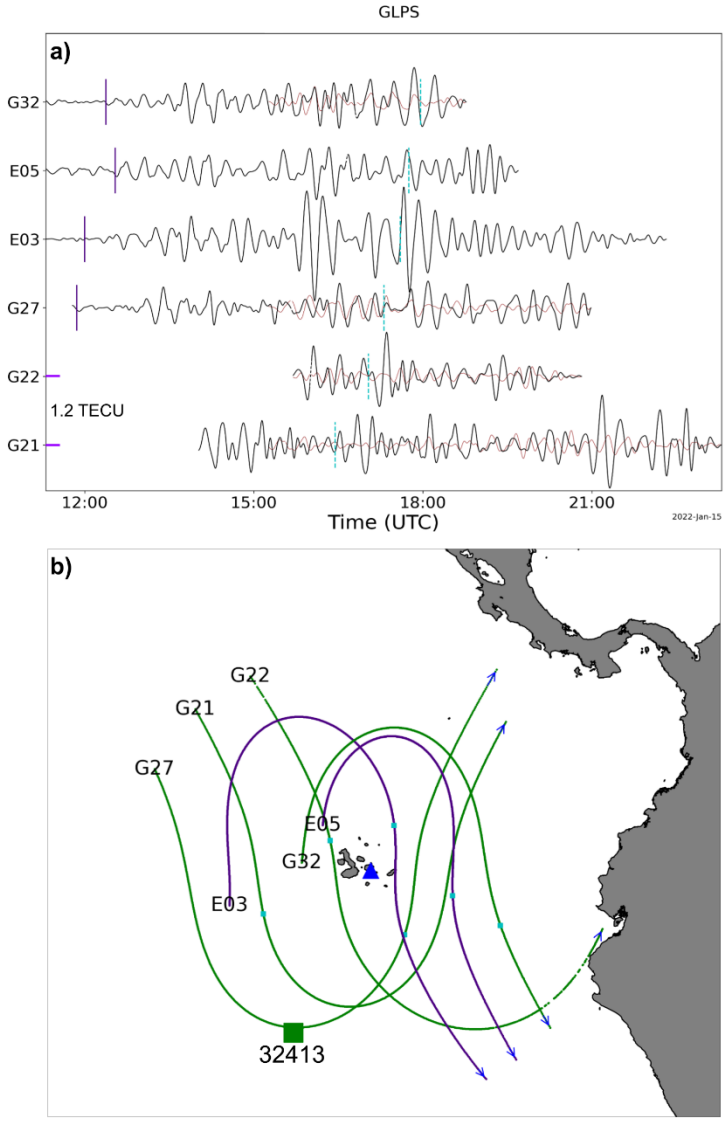

Figure S15. (a) The tsunami-induced ionospheric signatures detected in the vicinity of Galapagos Islands (GLPS GNSS receiver) following the passage of the tsunami triggered the HTHH volcanic eruption. **(b)** Geographic view of the GNSS receiver (red triangle) and the ionospheric tracks of the satellites whose sTEC time series are show in (a). The black square depicts the position of the tsunami buoy (DART 32413) used in Section 3.3 of the main text.

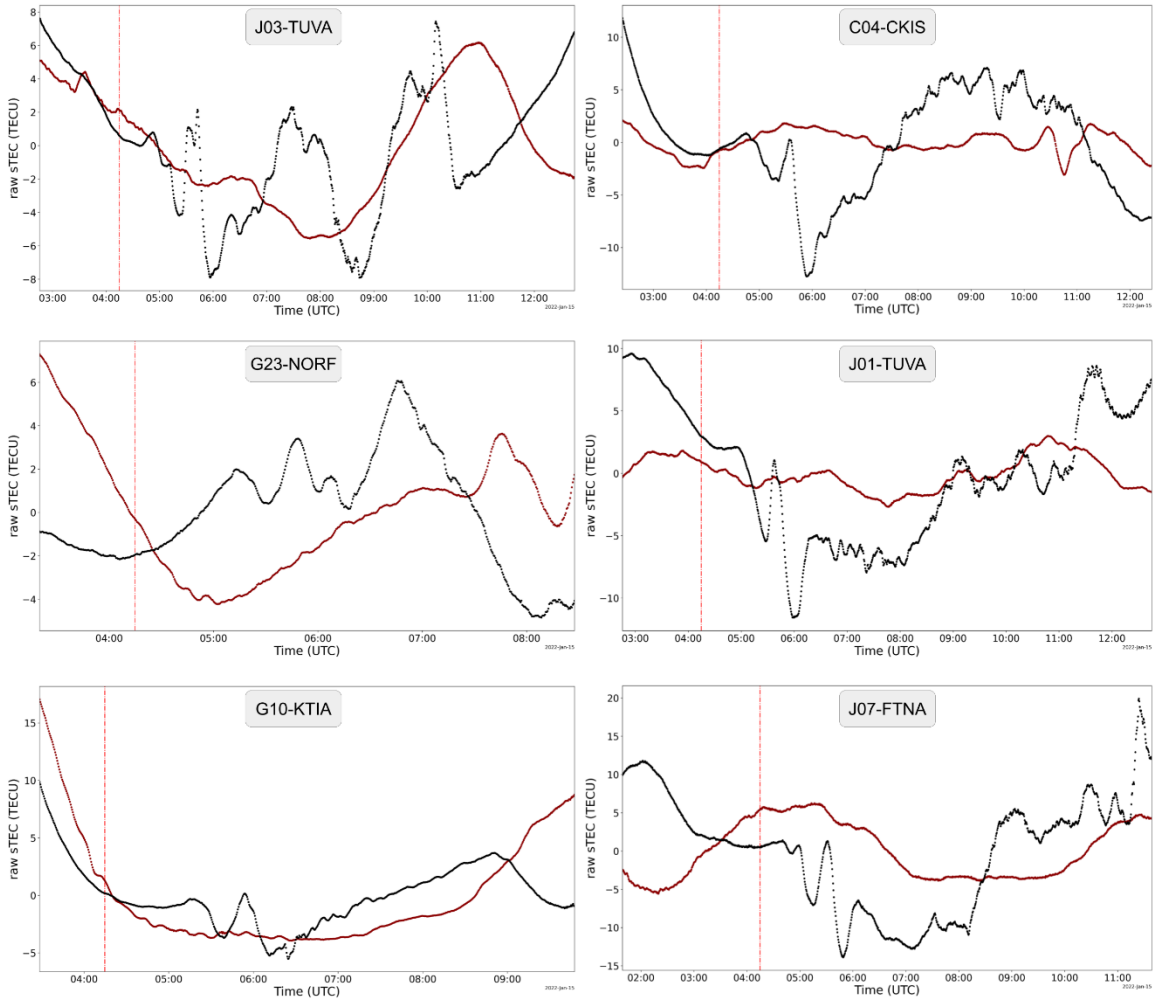

Figure S16. Raw ionospheric measurements during the eruption of the HTHH volcano to highlight the accompanied massive sTEC decreases and increases that resemble a large W-shape.

Contribution Statement:
Conceptualization: EM, LR
Methodology: EM, LR
Software: EM
Validation: EM, LR
Formal Analysis: EM
Investigation: EM, LR, AS
Writing - Original Draft: EM
Writing - Review and Editing: EM, LR, AS, BD
Visualization: EM
Supervision: LR, AS, BD

References

Artru, J., Ducic, V., Kanamori, H., Lognonné, P., & Murakami, M. (2005). Ionospheric detection of gravity waves induced by tsunamis. Geophys. J. Int, 160, 840–848. https://doi.org/10.1111/j.1365-246X.2005.02552.x

Calais, E., & Minster, J. B. (1995). Gps detection of ionospheric perturbations following the january 17, 1994, northridge earthquake. Geo-physical Research Letters, 22(9), 1045-1048. https://doi.org/10.1029/95GL00168

Davies, K., & Hartmann, G. K. (1997). Studying the ionosphere with the Global Positioning System. Radio Science, 32(4), 1695–1703. https://doi.org/10.1029/97RS00451

Davis, M. J. (1973). The integrated ionospheric response to internal atmospheric gravity waves. Journal of Atmospheric and Terrestrial Physics, 35(5), 929–959. https://doi.org/10.1016/0021-9169(73)90074-3

Donn, W. L., & Posmentier, E. S. (1964). Ground-coupled air waves from the great alaskan earthquake. Journal of Geophysical Research (1896-1977), 69(24), 5357-5361. https://doi.org/10.1029/JZ069i024p05357

Evans, J. V. (1957). The electron content of the ionosphere. Journal of Atmospheric and Terrestrial Physics, 11(3–4), 259–271. https://doi.org/10.1016/0021-9169(57)90071-5

Galvan, D. A., Komjathy, A., Hickey, M. P., & Mannucci, A. J. (2011). The 2009 Samoa and 2010 Chile tsunamis as observed in the ionosphere using GPS total electron content. Journal of Geophysical Research: Space Physics, 116(A6), n/a-n/a. https://doi.org/10.1029/2010JA016204

Hines, C. O. (1960). Internal atmospheric gravity waves at ionospheric heights. Canadian Journal of Physics, 38(11), 1441–1481. https://doi.org/10.1139/p60-150

Hines, C. O. (1972). Gravity Waves in the Atmosphere. Nature, 239 (5367), 73–78. https://doi.org/10.1038/239073a0

Hooke, W. H. (1969). E-region ionospheric irregularities produced by internal atmospheric gravity waves. Planetary and Space Science, 17(4), 749–765. https://doi.org/10.1016/0032-0633(69)90195-0

Liu, J. Y., Tsai, H. F., & Jung, T. K. (1996). Total Electron Content Obtained by Using the Global Positioning System. Terrestrial, Atmospheric and Oceanic Sciences, 7(1), 107. https://doi.org/10.3319/TAO.1996.7.1.107(A)

Liu, J. Y., Tsai, Y. B., Ma, K. F., Chen, Y. I., Tsai, H. F., Lin, C. H., . . . Lee, C. P. (2006). Ionospheric GPS total electron content (TEC) disturbances triggered by the 26 December 2004 Indian Ocean tsunami. Journal of Geophysical Research: Space Physics, 111 (5), 2–5. https://doi.org/10.1029/2005JA011200

Peltier, W. R., & Hines, C. O. (1976). On the possible detection of tsunamis by a monitoring of the ionosphere. Journal of Geophysical Research, 81(12), 1995–2000. https://doi.org/10.1029/jc081i012p01995

Ratcliffe, J. A. (1951). Some regularities in the F 2 region of the ionosphere. Journal of Geophysical Research, 56(4), 487–507. https://doi.org/10.1029/JZ056i004p00487

Ratcliffe, J. A. (1951). A quick method for analysing ionospheric records. Journal of Geophysical Research, 56(4), 463–485. https://doi.org/10.1029/JZ056i004p00463

Rolland, L. M., Occhipinti, G., Lognonn, P., & Loevenbruck, A. (2010). Ionospheric gravity waves detected offshore Hawaii after tsunamis. Geophysical Research Letters, 37(17). https://doi.org/10.1029/2010GL044479

Titheridge, J. E. (1972). Determination of ionospheric electron content from the Faraday rotation of geostationary satellite signals. Planetary and Space Science, 20(3), 353–369. https://doi.org/10.1016/0032-0633(72)90034-7

Zhang, S.-R., Fukao, S., Oliver, W. L., & Otsuka, Y. (1999). The height of the maximum ionospheric electron density over the MU radar. Journal of Atmospheric and Solar-Terrestrial Physics, 61(18), 1367–1383. https://doi.org/10.1016/S1364-6826(99)00088-7

Zhivetiev, I. (2019). gnss-tec (v1.1.1). https://github.com/gnss-lab/gnss-tec